

Article

Combustion Synthesis of Nanocrystalline Ba_{1.3}Ca_{0.7}SiO₄ Semiconductors Using Urea as an Energy Efficient Fuel

Desta R. Golja^{1,2}, Francis B. Dejene², Megersa K. Hussen³ and Jung Yong Kim^{4,5,*} ¹ Department of Physics and Nanotechnology, Salale University, Fiche P.O. Box 245, Ethiopia² Department of Chemical and Physical Sciences, Walter Sisulu University, Mthatha 5117, South Africa³ Department of Physics, Dire Dawa University, Dire Dawa P.O. Box 1362, Ethiopia⁴ Department of Materials Science and Engineering, Adama Science and Technology University, Adama P.O. Box 1888, Ethiopia⁵ Center of Advanced Materials Science and Engineering, Adama Science and Technology University, Adama P.O. Box 1888, Ethiopia

* Correspondence: jungyong.kim@astu.edu.et

Abstract: The τ -phase Ba_{1.3}Ca_{0.7}SiO₄ alkaline earth silicate powders were synthesized using the solution combustion technique. For this purpose, metal nitrate–urea mixtures were used as an oxidant and a fuel. Urea’s main function was to help lower the nominal combustion temperature (~550 °C) of the mixtures through exothermic reactions, leading to a relatively mild post-annealing temperature (~750 °C). If the urea concentration increased, the interconnected silicate particle size decreased with nanoscale crystallite (average, 33 ± 3 nm), affecting optical properties. Finally, the photoluminescence spectra suggested that the light emission was through trap sites, because the emitted blue and green lights (2.6 and 2.3 eV, respectively) were smaller than the bandgap (~3.2 eV) of the Ba_{1.3}Ca_{0.7}SiO₄ semiconductor.

Keywords: silicate; urea; metal oxide; semiconductor; photoluminescence; solution combustion synthesis



Citation: Golja, D.R.; Dejene, F.B.; Hussen, M.K.; Kim, J.Y. Combustion Synthesis of Nanocrystalline Ba_{1.3}Ca_{0.7}SiO₄ Semiconductors Using Urea as an Energy Efficient Fuel. *Inorganics* **2023**, *11*, 48. <https://doi.org/10.3390/inorganics11020048>

Academic Editor: Zemin Zhang

Received: 19 December 2022

Revised: 15 January 2023

Accepted: 16 January 2023

Published: 17 January 2023



Copyright: © 2023 by the authors. Licensee MDPI, Basel, Switzerland. This article is an open access article distributed under the terms and conditions of the Creative Commons Attribution (CC BY) license (<https://creativecommons.org/licenses/by/4.0/>).

1. Introduction

Silicate ceramic materials have received significant attention as a host matrix due to their several advantages, such as simple synthesis, durable crystal structure, thermal and chemical stability, environmental friendliness, and visible light transparency [1–3]. Silicates can have both amorphous and crystalline structures, and can be grouped as low, medium, and high melting point solids [1–4]. Therefore, it has been a topic of interest to study silicate materials by choosing an appropriate processing condition linked to the structure–property relationship. For example, Ca₂MgSi₂O₇, Sr₂MgSi₂O₇, and Sr₃MgSi₂O₈ were synthesized through a solid-state reaction at a sintering temperature of 1370 °C [5,6]. However, at this temperature, the reaction could be incomplete, suggesting the necessity of a higher temperature (1450 °C) with slow kinetics [7,8]. In addition, Sr₃SiO₅, Ca₃SiO₅, and Mg₃SiO₅ silicates were synthesized using a sol-gel method at 950 °C [6,9–12].

In the case of solution combustion synthesis, it was reported that very fine, homogenous, and crystalline samples could be obtained through the exothermic reactions between metal nitrate and fuel materials [11–21]. For example, the europium-doped (Ca_{2-x}Sr_x)MgSi₂O₇ (x = 0, 0.5, 1.5, and 2), Sr₃MgSi₂O₈, and Sr₂MgSi₂O₇ were synthesized by pre-heating at 500 °C and subsequent post-annealing at 900 °C [22,23]. This combustion process has advantages, such as simplicity, homogeneity, purity, short duration, and ease of scale-up, which should be suitable for versatile applications, such as luminescent diodes, fuel cells, energy conversion and storage devices [19,24–26]. Importantly, lower fusion temperatures open up opportunities for possibly more energy-efficient production processes.

In addition, combustion synthesis allows the ceramic powders to have agglomerated particles with $\sim 0.5\text{--}5\ \mu\text{m}$ diameters in their morphologies [27–29]. In this study, to tune the microstructure of the powder samples, the molar ratios of oxidizers and fuel were chosen to achieve a certain combustion temperature. This is because the heat generated from the exothermic reactions should be dependent on the fuel amounts and species [30–38]. The fuel species in combustion synthesis could be urea, glycine, citric acid, hydrazine, or carbohydrates, and their mixtures, in which a fuel has a partial solubility in an aqueous medium, for example, urea 1.08 g/mL in water [31–38]. In this paper, starting with the aforementioned silicate examples, we introduce our specific case, namely, $\text{Ba}_{1.3}\text{Ca}_{0.7}\text{SiO}_4$. Note that this complex silicate was first synthesized using the classical solid-state reaction in 1986 [39]. Here, we report the effect of urea (i.e., a type of fuel with high solubility in water and an appropriate decomposition temperature, $\sim 350\ \text{°C}$) [40,41] concentration on the thermal, structural, morphological, and photoluminescent properties of τ -phase $\text{Ba}_{1.3}\text{Ca}_{0.7}\text{SiO}_4$ semiconductors for lighting and light-emitting diode (LED) devices [42–44]. It was found that the urea concentration affected the microstructural morphologies and properties of the silicate semiconductor, an optical material. Importantly, the hexagonal $\text{Ba}_{1.3}\text{Ca}_{0.7}\text{SiO}_4$ compound is known to exhibit only a single τ -phase without a phase transformation, indicating that it is a very stable material and worthy of a fundamental study [39].

2. Results and Discussion

Figure 1 shows the thermal behavior of as-synthesized samples after burning at $550\ \text{°C}$ for $\sim 5\text{--}10$ min, according to the literature reports [11–17,19]. Here, Figure 1a–c denote the metal nitrate:urea (i.e., oxidant:fuel) ratios 1:0.75, 1:1.15, and 1:2.15, respectively, which correspond to the low, medium, and high concentrations of urea as a model composition, respectively [45]. As shown in Figure 1, there were two drastic decompositions at $\sim 25\text{--}100\ \text{°C}$ and $\sim 450\text{--}700\ \text{°C}$. The former was related to the desorption of residual small molecules (e.g., H_2O) due to the hygroscopic nature of the samples, whereas the latter originated in the further decomposition of the precursor and fuel materials (i.e., because of an incomplete combustion of samples at $550\ \text{°C}$). Here, it was noticeable that with increasing urea concentration, the differential thermal analysis (DTA) peak decreased from $669\ \text{°C}$ (metal nitrate:urea = 1:0.75) to $648\ \text{°C}$ (metal nitrate:urea = 1:1.15), and $631\ \text{°C}$ (metal nitrate:urea = 1:2.15). Note that urea has two hetero atoms (O and N) with lone pair electrons acting as a Lewis base. Hence, urea can undergo coordination bonding with the metal cations (Ca^{2+} and Ba^{2+}). Therefore, the DTA peaks observed in the range of $631\text{--}669\ \text{°C}$ might have been related to the decomposition of the nitrate clathrates (adducts). However, the corresponding decomposition peaks at lower temperatures ($<100\ \text{°C}$) were $91\ \text{°C}$, $94\ \text{°C}$, and $85\ \text{°C}$. On the other hand, when the molar ratio of metal nitrate:urea was 1:2.15, the corresponding peak was significantly downshifted to $85\ \text{°C}$. Furthermore, it was interesting to see an additional peak at $203\ \text{°C}$ when the molar ratio of metal nitrate:urea was 1:2.15 (i.e., a presence of incomplete decomposition during the fast exothermal reaction). Importantly, based on the thermogravimetric analysis (TGA) data in Figure 1, it was found that the post-annealing temperature should be greater than $700\ \text{°C}$ for $\text{Ba}_{1.3}\text{Ca}_{0.7}\text{SiO}_4$ silicate powders. Thus, in this study, we chose $750\ \text{°C}$ as a post-annealing temperature for complete decomposition of precursors such as $\text{Ba}(\text{NO}_3)_2$, $\text{Ca}(\text{NO}_3)_2$, $\text{Si}(\text{OC}_2\text{H}_5)_4$, and $\text{CH}_4\text{N}_2\text{O}$. Note that the final $\text{Ba}_{1.3}\text{Ca}_{0.7}\text{SiO}_4$ silicate powders were expected to be synthesized according to the below reaction (1), for which the precursor mixtures should have undergone the two-stage processing at $550\ \text{°C}$ and $750\ \text{°C}$ (at post-annealing) in the presence of the initial urea fuel ($n\text{CH}_4\text{NO}_2$, $n = 0.75\text{--}2.15$) [18–26,46,47]. Here, the byproducts could be 4NO_2 , O_2 , $2.8\text{H}_2\text{O}$, $2(\text{C}_2\text{H}_5)\text{O}$, etc., which were expected to further decompose into nitrogen, carbon, and hydrogen (i.e., a production of large amounts of gases, as reported regarding the solution combustion processes) [11–17,47].



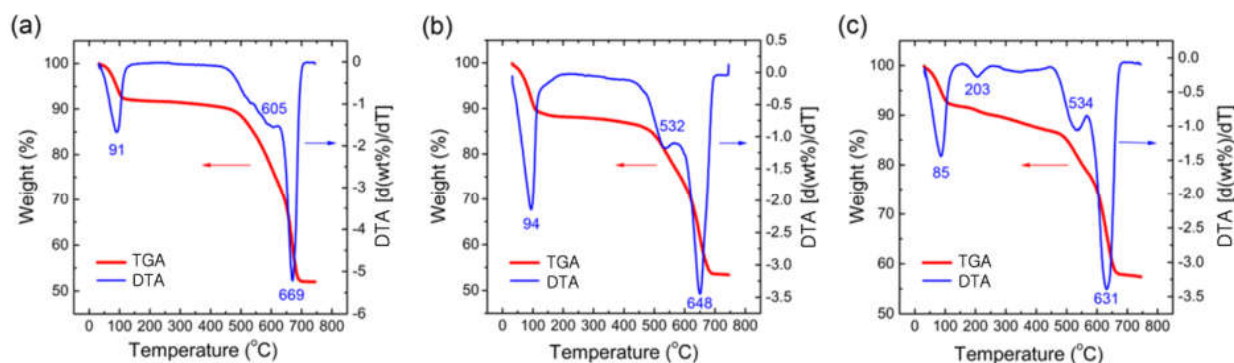


Figure 1. Thermogravimetric analysis (TGA) and differential thermal analysis (DTA) curves for the $\text{Ba}_{1.3}\text{Ca}_{0.7}\text{SiO}_4$ samples after burning at 550°C , at a heating rate of $10^\circ\text{C}/\text{min}$ under a N_2 flow of $80\text{ cm}^3/\text{min}$: (a) metal nitrate:urea = 1:0.75, (b) metal nitrate:urea = 1:1.15, and (c) metal nitrate:urea = 1:2.15.

Figure 2 shows the Fourier transform infrared (FT-IR) spectra for the samples after burning at 550°C ; Figure 2a–c correspond to metal nitrate:urea = 1:0.75, 1:1.15, and 1:2.15 samples, respectively. As shown in Figure 2, O-H stretching (from adsorbed water) was observed at 3648 cm^{-1} , whereas N-H stretching and N-O stretching were displayed at 2207 cm^{-1} and 1434 cm^{-1} , respectively. Furthermore, Si-O stretching, Si-O-Si bending, Ba-O stretching, and Ca-O stretching were exhibited at 970 cm^{-1} , 835 cm^{-1} , 725 cm^{-1} , and 673 cm^{-1} , respectively. Interestingly, when the urea concentration was relatively high (see Figure 2c), small peaks were additionally observed, displaying the presence of trivial decomposed molecules due to the rapid and intensive exothermic reactions in this sample. Recall also the additional DTA peak at 203°C in Figure 1c.

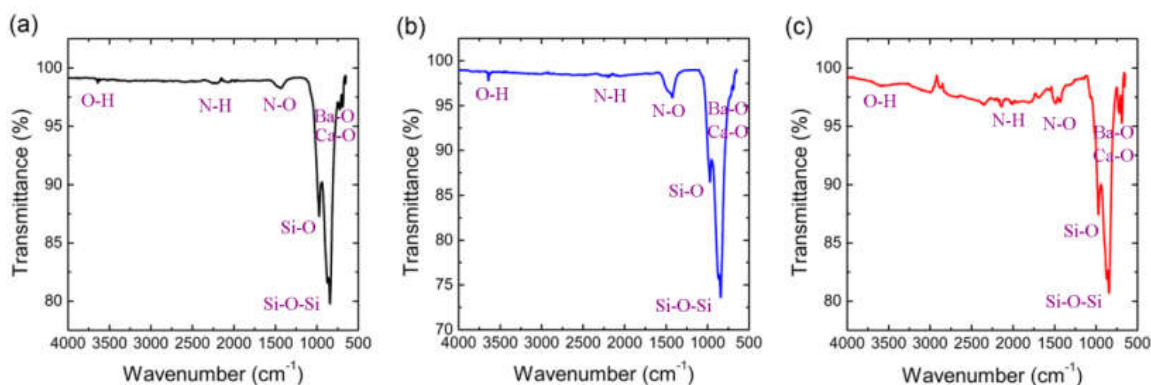


Figure 2. FTIR spectra of $\text{Ba}_{1.3}\text{Ca}_{0.7}\text{SiO}_4$ samples burned at 550°C : (a) metal nitrate:urea = 1:0.75, (b) metal nitrate:urea = 1:1.15, and (c) metal nitrate:urea = 1:2.15.

As shown in Figures 1 and 2, the combustion reaction at 550°C was insufficient for a complete reaction, indicating further annealing was needed, at higher than 700°C . Hence, we chose the post-annealing temperature of 750°C for 2 h. We then characterized the X-ray diffraction (XRD) patterns of the $\text{Ba}_{1.3}\text{Ca}_{0.7}\text{SiO}_4$ samples as a function of the molar ratio of metal nitrate:urea (see Figure 3). The first observation was that all the diffraction peaks were consistent with that of τ -phase hexagonal $\text{Ba}_{1.3}\text{Ca}_{0.7}\text{SiO}_4$ (JCPDS, No. 36-1449) [39]. Here, the crystallite size (t) of $\text{Ba}_{1.3}\text{Ca}_{0.7}\text{SiO}_4$ samples could be estimated through the Scherrer equation,

$$t = \frac{0.9 \cdot \lambda}{\beta \cos \theta} \quad (2)$$

where $\lambda = 0.154$ nm is the wavelength of x-ray, and β is the full-width at half maximum (FWHM) at the diffraction angle, θ . The results are summarized in Table 1 and Figure 4. As shown in Figure 4, the crystallite size initially decreased with increasing urea concentration up to nitrate:urea = 1:1.15, and then leveled off. However, a similar crystallite size (~31.2–31.0 nm) does not necessarily mean an indistinguishable property, which demanded further characterization of the samples. Furthermore, the experimental XRD data were shifted to the left compared with the JCPDS #36-1499 prediction. For example, the d -spacing at the (102) crystallographic plane was 0.290 nm (experiment at $2\theta = 30.8^\circ$) and 0.287 nm (JCPDS at $2\theta = 31.1^\circ$), respectively, based on Bragg's law ($\lambda = 2d \cdot \sin \theta$). Hence, this comparison indicated that the interplanar distance should have been partially expanded due to drastic exothermic reactions when the solution combustion synthesis was employed.

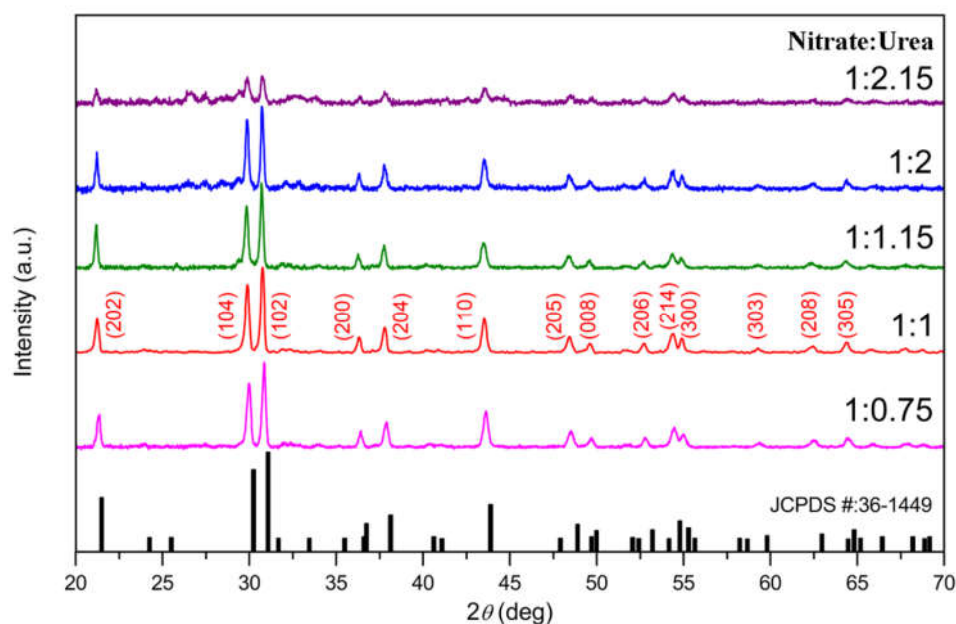


Figure 3. XRD spectra of τ -phase $\text{Ba}_{1.3}\text{Ca}_{0.7}\text{SiO}_4$ powder samples as a function of the molar ratio of metal nitrate:urea (after post-annealing at 750°C for 2 h).

Table 1. Crystallite size (t) of τ -phase $\text{Ba}_{1.3}\text{Ca}_{0.7}\text{SiO}_4$ silicate powders at $\theta = 15.42^\circ$, i.e., (101) crystallographic plane. Here, β denotes a full width at half maximum (FWHM).

	Metal Nitrate: Urea (Molar Ratios)				
	1:0.75	1:1	1:1.15	1:2	1:2.15
β (radian)	0.00377	0.00419	0.00461	0.00461	0.00464
t (nm)	38.1	34.3	31.2	31.2	31.0

Figure 5 shows (a) the excitation and (b) emission spectra of the nanocrystalline $\text{Ba}_{1.3}\text{Ca}_{0.7}\text{SiO}_4$ samples as a function of the metal nitrate:urea molar ratio (after post-annealing at 750°C for 2 h). First, note that the τ -phase $\text{Ba}_{1.3}\text{Ca}_{0.7}\text{SiO}_4$ samples had an optical bandgap of ca. 3.2 eV, corresponding to ~ 390 nm [41]. Hence, the excitation peaks at 316 nm, 340 nm, and 393 nm in Figure 5a were related to the electronic structure of $\text{Ba}_{1.3}\text{Ca}_{0.7}\text{SiO}_4$. However, the emission lights at 487 nm (~ 2.6 eV) and 537 nm (~ 2.3 eV) had smaller energies than the bandgap (~ 3.2 eV) of the silicate samples did, suggesting that the emissions did not originate from a band-to-band transition, but from a band-to-trap (or

trap-to-trap or trap-to-band) transition. Here, hole-/electron-traps indicated a defect site in the silicate samples.

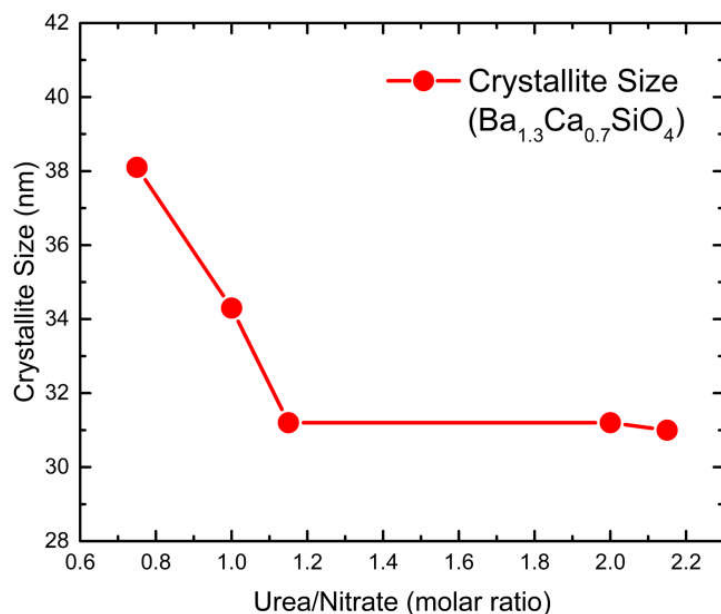


Figure 4. Crystallite size of τ -phase $\text{Ba}_{1.3}\text{Ca}_{0.7}\text{SiO}_4$ powder samples as a function of the molar ratio of metal nitrate:urea.

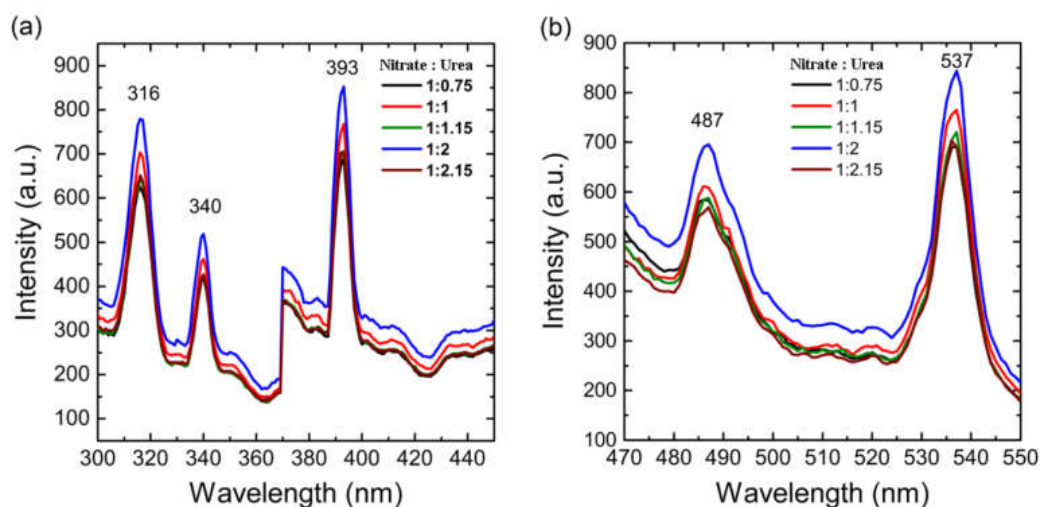


Figure 5. Photoluminescence properties of (a) excitation and (b) emission of τ -phase $\text{Ba}_{1.3}\text{Ca}_{0.7}\text{SiO}_4$ powder samples.

Therefore, based on the aforementioned photoluminescence (PL) results, a PL mechanism was suggested, as shown in Figure 6. When the wide bandgap $\text{Ba}_{1.3}\text{Ca}_{0.7}\text{SiO}_4$ silicate was excited through photon absorption, the electrons in the conduction band (CB) could recombine with holes in the hole trap site for light emission. Similarly, the electron trap-to-valence band (VB) and trap-to-trap transition could be possible reasons for PL emission.

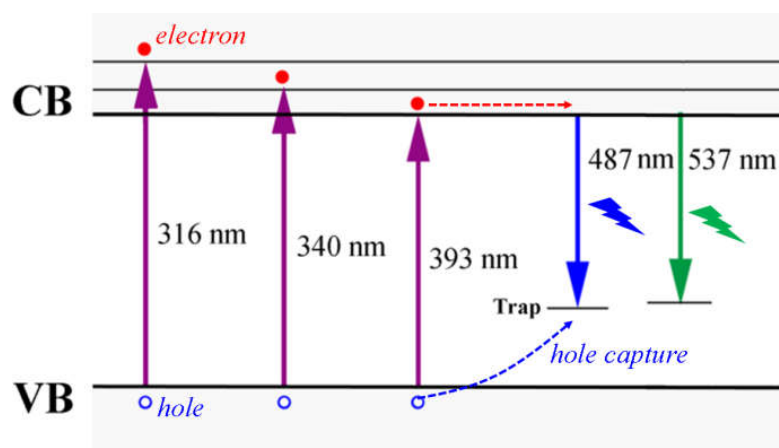


Figure 6. Photoluminescence (PL) process in τ -phase $\text{Ba}_{1.3}\text{Ca}_{0.7}\text{SiO}_4$ powder samples, suggesting the recombination should be related with the trap sites. Note that here, only hole traps were drawn for simplicity.

Figure 7 shows the scanning electron microscopy (SEM) images for τ -phase $\text{Ba}_{1.3}\text{Ca}_{0.7}\text{SiO}_4$ samples when the molar ratios of metal nitrate:urea were (a) 1:0.75, (b) 1:1.15, and (c) 1:2.15. As shown in Figure 7, when the urea amount was low, the microstructural morphology appeared rod-like. However, when the urea amount was medium, the morphology appeared plate-like. Finally, when the urea amount was high, the morphology changed drastically, exhibiting inter-connected granular particles with some pores (due to a rapid escape of volatile gas molecules). Note that the average crystallite sizes of (b) and (c) were similar (i.e., (b) 31.2 nm and (c) 31.0 nm, respectively, as shown in Figure 3), because the crystallite size was partially polycrystals. This indicated that although the microscale particle size was different, the small crystallite domains could be similar, as in (b) and (c) (recall Figure 4 and Table 1). Finally, Figure 8 displays both the energy-dispersive X-ray spectroscopy (EDX) spectra (a, b, and c) and elemental mapping (d, e, and f) for the τ -phase $\text{Ba}_{1.3}\text{Ca}_{0.7}\text{SiO}_4$ samples, confirming that the silicate samples were composed of Ba, Ca, Si, and O atoms. However, the compound was synthesized via a small-scale explosive reaction (i.e., solution combustion synthesis). Hence, the versatile surface defects may have affected some of the EDX results; however, a trace of aluminum was also observed as an impurity due to the alumina crucible used for the combustion synthesis process.

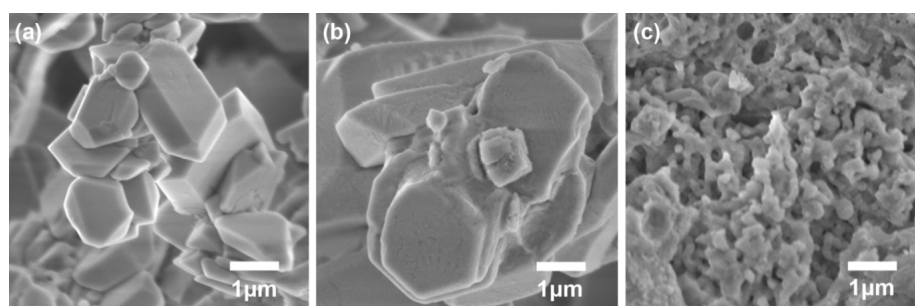


Figure 7. The SEM images for τ -phase $\text{Ba}_{1.3}\text{Ca}_{0.7}\text{SiO}_4$ samples when the molar ratios of metal nitrate:urea were (a) 1:0.75, (b) 1:1.15, and (c) 1:2.15.

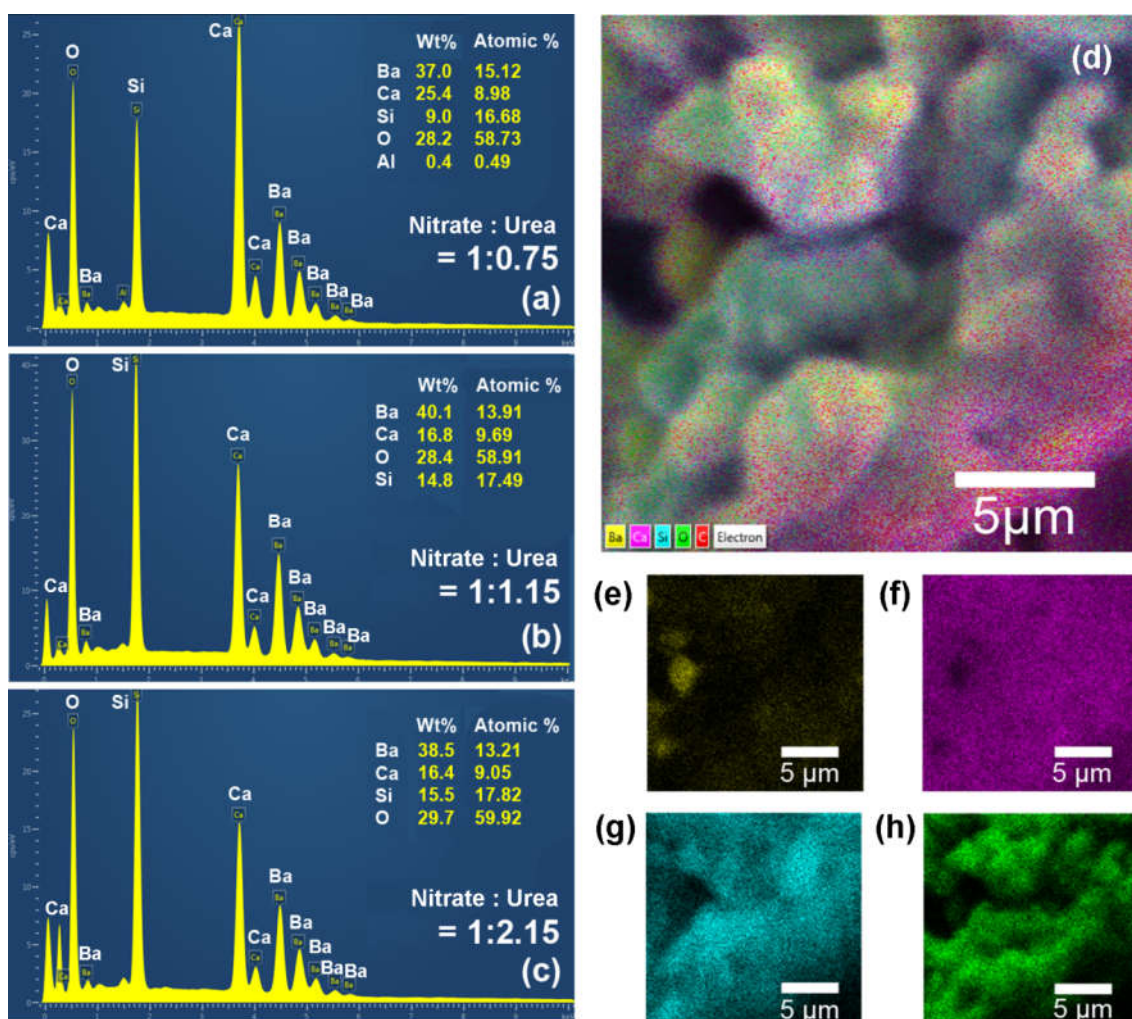


Figure 8. The EDX spectra for τ -phase $\text{Ba}_{1.3}\text{Ca}_{0.7}\text{SiO}_4$ powder samples when the molar ratios of metal nitrate:urea were (a) 1:0.75, (b) 1:1.15, and (c) 1:2.15. The EDX elemental mapping of τ -phase $\text{Ba}_{1.3}\text{Ca}_{0.7}\text{SiO}_4$: (d) a layered sample, (e) barium, (f) calcium, (g) silicon, and (h) oxygen.

3. Materials and Methods

The τ -phase $\text{Ba}_{1.3}\text{Ca}_{0.7}\text{SiO}_4$ silicate powders were synthesized as a function of urea concentration using a solution/gel combustion method. The precursor materials were $\text{Ba}(\text{NO}_3)_2$ (99.9%; molar mass = 261.35 g/mol), $\text{Ca}(\text{NO}_3)_2 \cdot 4\text{H}_2\text{O}$ (99.9%; molar mass = 236.15 g/mol), $\text{Si}(\text{OC}_2\text{H}_5)_4$ (99.99%; molar mass = 208.33 g/mol), and $\text{CH}_4\text{N}_2\text{O}$ (99.9%; molar mass = 60.06 g/mol), which were obtained from Sigma-Aldrich and used as received without further purification. All precursors with the molar ratios of metal nitrate:urea in the range of 1:0.75–1:2.15 were mixed in 10 mL deionized water. Specifically, the stoichiometric amounts of 1.000 g of $\text{Ba}(\text{NO}_3)_2$, 0.487 g of $\text{Ca}(\text{NO}_3)_2 \cdot 4\text{H}_2\text{O}$, 0.614 g of $\text{Si}(\text{OC}_2\text{H}_5)_4$, and 0.265 g (to 0.766 g) of $\text{CH}_4\text{N}_2\text{O}$ were dissolved into water and continuously stirred for 30 min. Next, the solution was heated at 80 °C until a transparent solution formed. Finally, the precursor mixture was transferred to an alumina crucible and quickly inserted into a pre-heated 8 L muffle furnace heated at 550 °C for ~5–10 min. The mixture then self-ignited with a white flame, leading to a highly porous foamy solid product. Finally, the powder samples were post-annealed at 750 °C for 2 h, resulting in τ -phase $\text{Ba}_{1.3}\text{Ca}_{0.7}\text{SiO}_4$ alkaline earth silicate powders.

Thermogravimetric analysis (TGA) and differential thermal analysis (DTA) were carried out using a TGA/DTA thermal analyzer (NETZSCH STA 449 C, Selb, Germany) with N_2 flow at the heating rate of 10 °C/min. The functional groups of materials were analyzed using a Fourier transform infrared (FT-IR) spectrophotometer (IRAffinity-1S, Shimadzu).

X-ray diffraction (XRD) patterns for the samples were identified using a D8 advanced Bruker diffractometer with a detector (12 mm × 16 mm) suitable for CuK α ($\lambda = 1.54060 \text{ \AA}$) irradiation, operating at an applied voltage of 45 kV with a current intensity of 40 mA, during which XRD data were collected in the range of $2\theta = 20\text{--}70^\circ$. Note that the accuracy and reproducibility of XRD are 0.005° and 0.0002° , respectively. The microstructural morphologies of the powder samples were analyzed using a PHI700 nanoprobe and Shimadzu model ZU SSX-550 super scanning electron microscopy (SEM) coupled with energy-dispersive X-ray spectroscopy (EDX) (Oxford x-Max N). EDX was used to determine the elemental analysis and chemical composition of the samples. The photoluminescence (PL) spectra of synthesized samples were recorded on a Hitachi F-7000 phosphorescence spectrometer. Note that all the characterizations were carried out at $\sim 23^\circ\text{C}$.

4. Conclusions

The Ba_{1.3}Ca_{0.7}SiO₄ semiconductors were prepared through combustion synthesis, for which urea was employed as a fuel with the molar ratios of metal nitrate:urea = 1:0.75, 1:1.15, and 1:2.15. First, the TGA results indicated that when the urea ratio increased from 1:0.75 to 1:1.15 and 1:2.15, the main decomposition temperature decreased from 669 °C to 648 °C and 631 °C, respectively, indicating urea's role as a fuel during the exothermic reactions. Second, the FT-IR spectra demonstrated the presence of the main functional groups, such as Si-O, N-H, Ba-O, and Ca-O. Third, the XRD patterns indicated that the silicate Ba_{1.3}Ca_{0.7}SiO₄ had a τ -phase hexagonal structure with an average crystallite size of $\sim 33 \pm 3 \text{ nm}$. When the molar ratio of metal nitrate:urea was greater than 1:1.15, the crystallite size levelled off at $\sim 31 \text{ nm}$. Fourth, the PL spectra showed that the blue/green light emission was processed through trap sites because the recombination energy ($\sim 2.3\text{--}2.6 \text{ eV}$) was smaller than the bandgap ($\sim 3.2 \text{ eV}$) of silicate samples. Fifth, according to SEM results, the aggregated particle size decreased with increasing urea concentration. Sixth, EDX spectra confirmed the elemental components (Ba, Ca, Si, and O) of the Ba_{1.3}Ca_{0.7}SiO₄ silicate powders. Finally, it was proven that Ba_{1.3}Ca_{0.7}SiO₄ silicate powders could be synthesized at a post-annealing temperature of 750 °C after burning the samples at 550 °C.

Author Contributions: Conceptualization, F.B.D. and J.Y.K.; methodology, D.R.G., F.B.D., M.K.H. and J.Y.K.; formal analysis, D.R.G., F.B.D., M.K.H. and J.Y.K.; investigation, D.R.G.; resources, F.B.D.; data curation, D.R.G. and M.K.H.; writing—original draft preparation, D.R.G.; writing—review and editing, J.Y.K.; supervision, F.B.D. and J.Y.K.; funding acquisition, D.R.G. and F.B.D. All authors have read and agreed to the published version of the manuscript.

Funding: This research received no external funding. The APC was funded by JYK.

Data Availability Statement: The datasets used and/or analyzed during the current study are available from the corresponding author upon reasonable request.

Acknowledgments: We acknowledge financial support from the Ministry of Education in Ethiopia and the National Research Foundation of South Africa.

Conflicts of Interest: The authors declare no competing interests.

References

1. Mondal, K.; Kumari, P.; Manam, J. Influence of doping and annealing temperature on the structural and optical properties of Mg₂SiO₄: Eu³⁺ synthesized by combustion method. *Curr. Appl. Phys.* **2016**, *16*, 707–719. [[CrossRef](#)]
2. Naik, R.; Prashantha, S.; Nagabhushana, H.; Sharma, S.; Nagabhushana, B.; Nagaswarupa, H.; Premkumar, H. Low temperature synthesis and photoluminescence properties of red emitting Mg₂SiO₄: Eu³⁺ nanophosphor for near UV light emitting diodes. *Sens. Actuators B Chem.* **2014**, *195*, 140–149. [[CrossRef](#)]
3. Hiramatsu, H.; Yusa, H.; Igarashi, R.; Ohishi, Y.; Kamiya, T.; Hosono, H. An exceptionally narrow band-gap ($\sim 4 \text{ eV}$) silicate predicted in the cubic perovskite structure: BaSiO₃. *Inorg. Chem.* **2017**, *56*, 10535–10542. [[CrossRef](#)] [[PubMed](#)]
4. AlOthman, Z.A. A Review: Fundamental Aspects of Silicate Mesoporous Materials. *Materials* **2012**, *5*, 2874–2902. [[CrossRef](#)]
5. Wu, C.; Chang, J.; Ni, S.; Wang, J. In vitro bioactivity of akermanite ceramics. *J. Biomed. Mater. Res. Part A* **2006**, *76*, 73–80. [[CrossRef](#)]

6. Alvani, A.S.; Moztarzadeh, F.; Sarabi, A. Effects of dopant concentrations on phosphorescence properties of Eu/Dy-doped $\text{Sr}_3\text{MgSi}_2\text{O}_8$. *J. Lumin.* **2005**, *114*, 131–136. [[CrossRef](#)]
7. Pan, W.; Ning, G.-L.; Wang, J.-H.; Lin, Y. A novel synthesis of alkaline earth silicate phosphor $\text{Sr}_3\text{MgSi}_2\text{O}_8$: Eu^{2+} , Dy^{3+} . *Chin. J. Chem.* **2007**, *25*, 605–608. [[CrossRef](#)]
8. Pritts, I.M.; Daugherty, K.E. The effect of stabilizing agents on the hydration rate of β -C2S. *Cem. Concr. Res.* **1976**, *6*, 783–795. [[CrossRef](#)]
9. Nettleship, I.; Shull, J.L.; Kriven, W.M. Chemical preparation and phase stability of Ca_2SiO_4 and Sr_2SiO_4 powders. *J. Eur. Ceram. Soc.* **1993**, *11*, 291–298. [[CrossRef](#)]
10. Singh, D.; Sheoran, S.; Bhagwan, S.; Kadyan, S. Optical characteristics of sol-gel derived M_3SiO_5 : Eu^{3+} (M= Sr, Ca and Mg) nanophosphors for display device technology. *Cogent Phys.* **2016**, *3*, 1262573. [[CrossRef](#)]
11. Varma, A.; Mukasyan, A.S.; Rogachev, A.S.; Manukyan, K.V. Solution combustion synthesis of nanoscale materials. *Chem. Rev.* **2016**, *116*, 14493–14586. [[CrossRef](#)]
12. Patil, K.C.; Aruna, S.; Mimani, T. Combustion synthesis: An update. *Curr. Opin. Solid State Mater. Sci.* **2002**, *6*, 507–512. [[CrossRef](#)]
13. Wen, W.; Wu, J.-M. Nanomaterials via solution combustion synthesis: A step nearer to controllability. *RSC Adv.* **2014**, *4*, 58090–58100. [[CrossRef](#)]
14. Siddique, F.; Gonzalez-Cortes, S.; Mirzaei, A.; Xiao, T.; Rafiq, M.A.; Zhang, X. Solution combustion synthesis: The relevant metrics for producing advanced and nanostructured photocatalysts. *Nanoscale* **2022**, *14*, 11806–11868. [[CrossRef](#)]
15. Deganello, F.; Tyagi, A.K. Solution combustion synthesis, energy and environment: Best parameters for better materials. *Prog. Cryst. Growth Charact. Mater.* **2018**, *64*, 23–61. [[CrossRef](#)]
16. Novitskaya, E.; Kelly, J.P.; Bhaduri, S.; Graeve, O.A. A review of solution combustion synthesis: An analysis of parameters controlling powder characteristics. *Int. Mater. Rev.* **2020**, *66*, 188–214. [[CrossRef](#)]
17. Aruna, S.T.; Mukasyan, A.S. Combustion synthesis and nanomaterials. *Curr. Opin. Solid State Mater. Sci.* **2008**, *12*, 44–50. [[CrossRef](#)]
18. Kingsley, J.J.; Manickam, N.; Patil, K.C. Combustion synthesis and properties of fine particle fluorescent aluminous oxides. *Bull. Mater. Sci.* **1990**, *13*, 179–189. [[CrossRef](#)]
19. Kingsley, J.; Patil, K. A novel combustion process for the synthesis of fine particle α -alumina and related oxide materials. *Mater. Lett.* **1988**, *6*, 427–432. [[CrossRef](#)]
20. Qiu, Z.; Zhou, Y.; Lü, M.; Zhang, A.; Ma, Q. Combustion synthesis of long-persistent luminescent MAl_2O_4 : Eu^{2+} , R^{3+} (M = Sr, Ba, Ca, R = Dy, Nd and La) nanoparticles and luminescence mechanism research. *Acta Mater.* **2007**, *55*, 2615–2620. [[CrossRef](#)]
21. Raza, M.A.; Rahman, I.Z.; Beloshapkin, S. Synthesis of nanoparticles of $\text{La}_{0.75}\text{Sr}_{0.25}\text{Cr}_{0.5}\text{Mn}_{0.5}\text{O}_{3-\delta}$ (LSCM) perovskite by solution combustion method for solid oxide fuel cell application. *J. Alloys Compd.* **2009**, *485*, 593–597. [[CrossRef](#)]
22. Bhatkar, V.B.; Bhatkar, N.V. Combustion synthesis and photoluminescence study of silicate biomaterials. *Bull. Mater. Sci.* **2011**, *34*, 1281–1284. [[CrossRef](#)]
23. Talwar, G.; Joshi, C.; Moharil, S.; Dhopte, S.; Muthal, P.; Kondawar, V. Combustion synthesis of $\text{Sr}_3\text{MgSi}_2\text{O}_8$: Eu^{2+} and $\text{Sr}_2\text{MgSi}_2\text{O}_7$: Eu^{2+} phosphors. *J. Lumin.* **2009**, *129*, 1239–1241. [[CrossRef](#)]
24. Thoda, O.; Xanthopoulou, G.; Vekinis, G.; Chronos, A. Review of recent studies on solution combustion synthesis of nanostructured catalysts. *Adv. Eng. Mater.* **2018**, *20*, 1800047. [[CrossRef](#)]
25. Carlos, E.; Martins, R.; Fortunato, E.; Branquinho, R. Solution combustion synthesis: Towards a sustainable approach for metal oxides. *Chem. Eur. J.* **2020**, *26*, 9099–9125. [[CrossRef](#)]
26. Branquinho, R.; Santa, A.; Carlos, E.; Salgueiro, D.; Barquinha, P.; Martins, R.; Fortunato, E. *Developments in Combustion Technology*; Kyprianidis, K.G., Skvaril, J., Eds.; InTechOpen: Rijeka, Croatia, 2016; pp. 397–417. [[CrossRef](#)]
27. Kelkar, S.A.; Shaikh, P.A.; Pachfule, P.; Ogale, S.B. Nanostructured Cd_2SnO_4 as an energy harvesting photoanode for solar water splitting. *Energy Environ. Sci.* **2012**, *5*, 5681–5685. [[CrossRef](#)]
28. Wen, W.; Wu, J.-M.; Tu, J.-P. A novel solution combustion synthesis of cobalt oxide nanoparticles as negative-electrode materials for lithium ion batteries. *J. Alloys Compd.* **2012**, *513*, 592–596. [[CrossRef](#)]
29. Ekambaram, S.; Patil, K.C. Synthesis and properties of rare earth doped lamp phosphors. *Bull. Mater. Sci.* **1995**, *18*, 921–930. [[CrossRef](#)]
30. Amosov, A.P.; Novikov, V.A.; Kachkin, E.M.; Kryukov, N.A.; Titov, A.A.; Sosnin, I.M.; Merson, D.L. The Solution Combustion Synthesis of ZnO Powder for the Photodegradation of Phenol. *Ceramics* **2022**, *5*, 928–946. [[CrossRef](#)]
31. Mokkelbost, T.; Kaus, I.; Grande, T.; Einarsrud, M.-A. Combustion synthesis and characterization of nanocrystalline CeO_2 -based powders. *Chem. Mater.* **2004**, *16*, 5489–5494. [[CrossRef](#)]
32. Jiang, Y.; Yang, S.; Hua, Z.; Huang, H. Sol-gel auto combustion synthesis of metals and metal alloys. *Angew. Chem. Int. Ed.* **2009**, *48*, 8529–8531. [[CrossRef](#)]
33. Bera, P.; Hegde, M. Characterization and catalytic properties of combustion synthesized Au/ CeO_2 catalyst. *Catal. Lett.* **2002**, *79*, 75–81. [[CrossRef](#)]
34. Ianoş, R.; Tăculescu, A.; Păcurariu, C.; Lazău, I. Solution combustion synthesis and characterization of magnetite, Fe_3O_4 , Nanopowders. *J. Am. Ceram. Soc.* **2012**, *95*, 2236–2240. [[CrossRef](#)]
35. Voskanyan, A.A.; Chan, K. Solution combustion synthesis using furfuryl alcohol as fuel and a combustible solvent. *J. Exp. Nanosci.* **2015**, *10*, 466–475. [[CrossRef](#)]

36. Valefi, M.; Falamaki, C.; Ebadzadeh, T.; Hashjin, M.S. New insights of the glycine-nitrate process for the synthesis of nano-crystalline 8YSZ. *J. Am. Ceram. Soc.* **2007**, *90*, 2008–2014. [[CrossRef](#)]
37. Thompson, J.G.; Withers, R.L.; Hyde, B.G. Further consideration of phases in the system Ba₂SiO₄-Ca₂SiO₄. *J. Am. Ceram. Soc.* **1987**, *70*, C-383–C-386. [[CrossRef](#)]
38. Ianoș, R.; Muntean, E.; Lazău, R.; Băbuță, R.; Moacă, E.-A.; Păcurariu, C.; Dabici, A.; Hulka, I. One-step synthesis of near-infrared reflective brown pigments based on iron-doped lanthanum aluminate, LaAl_{1-x}FexO₃. *Dye. Pigment.* **2018**, *152*, 105–111. [[CrossRef](#)]
39. Matkovic, B.; Popović, S.; Grzeta, B.; Halle, R. Phases in the system Ba₂SiO₄-Ca₂SiO₄. *J. Am. Ceram. Soc.* **1986**, *69*, 132–134. [[CrossRef](#)]
40. Yim, S.D.; Kim, S.J.; Baik, A.J.H.; Nam, I.-S.; Mok, Y.S.; Lee, J.-H.; Cho, B.K.; Oh, S.H. Decomposition of urea into NH₃ for the SCR process. *Ind. Eng. Chem. Res.* **2004**, *43*, 4856–4863. [[CrossRef](#)]
41. Wang, D.; Dong, N.; Hui, S.; Niu, Y. Analysis of urea pyrolysis products in 132.5–190 °C. *Energy Procedia* **2019**, *158*, 2170–2175. [[CrossRef](#)]
42. Golja, D.R.; Dejene, F.B.; Kim, J.Y. Trivalent rare-earth-codoped silicate phosphor materials (Ba_{1.3}Ca_{0.7-x-y}SiO₄: xDy³⁺/yEu³⁺) for solid-state lighting. *J. Phys. Condens. Matter* **2022**, *34*, 294006. [[CrossRef](#)] [[PubMed](#)]
43. Golja, D.R.; Dejene, F.B.; Kim, J.Y. Single-phase silicate phosphors (Ba_{1.3}Ca_{0.7-x}SiO₄:xDy³⁺) doped with dysprosium for white solid-state lighting. *Adv. Condens. Matter Phys.* **2022**, *2022*, 4317275. [[CrossRef](#)]
44. Golja, D.R.; Woldemariam, M.M.; Dejene, F.B.; Kim, J.Y. Photoluminescence processes in τ-phase Ba_{1.3}Ca_{0.7-x-y}SiO₄:xDy³⁺/yTb³⁺ phosphors for solid-state lighting. *R. Soc. Open Sci.* **2022**, *9*, 220101. [[CrossRef](#)] [[PubMed](#)]
45. Mukasyan, A.S.; Costello, C.; Sherlock, K.P.; Lafarga, D.; Varma, A. Perovskite Membranes by Aqueous Combustion Synthesis: Synthesis and Properties. *Sep. Purif. Technol.* **2001**, *25*, 117–126. [[CrossRef](#)]
46. Wynne, A.M. The thermal decomposition of urea: An undergraduate thermal analysis experiment. *J. Chem. Educ.* **1987**, *64*, 180–182. [[CrossRef](#)]
47. Fang, H.L.; DaCosta, H.F. Urea thermolysis and NO_x reduction with and without SCR catalysts. *Appl. Catal. B Environ.* **2003**, *46*, 17–34. [[CrossRef](#)]

Disclaimer/Publisher's Note: The statements, opinions and data contained in all publications are solely those of the individual author(s) and contributor(s) and not of MDPI and/or the editor(s). MDPI and/or the editor(s) disclaim responsibility for any injury to people or property resulting from any ideas, methods, instructions or products referred to in the content.